nature materials

LETTERS

PUBLISHED ONLINE: 29 JUNE 2015 | DOI: 10.1038/NMAT4336

In situ study of the initiation of hydrogen bubbles at the aluminium metal/oxide interface

De-Gang Xie[1], Zhang-Jie Wang[1], Jun Sun[1], Ju Li[1,2,3]*, Evan Ma[1,4]* and Zhi-Wei Shan[1]*

The presence of excess hydrogen at the interface between a metal substrate and a protective oxide can cause blistering[1–3] and spallation of the scale[4–8]. However, it remains unclear how nanoscale bubbles manage to reach the critical size in the first place. Here, we perform *in situ* environmental transmission electron microscopy experiments of the aluminium metal/oxide interface under hydrogen exposure. It is found that once the interface is weakened by hydrogen segregation, surface diffusion of Al atoms initiates the formation of faceted cavities on the metal side, driven by Wulff reconstruction. The morphology and growth rate of these cavities are highly sensitive to the crystallographic orientation of the aluminium substrate. Once the cavities grow to a critical size, the internal gas pressure can become great enough to blister the oxide layer. Our findings have implications for understanding hydrogen damage of interfaces.

Hydrogen-induced interfacial failure, such as blistering at the metal (M)/oxide (MO) interface and protective scale spallation, is well known to plague native oxides and coatings on metals and alloys. In gas turbines[3,6–8], nuclear power plants[9–11], humid environments[1,12], or even solar sails[13], such hydrogen-related damage can be severe. It is generally believed that gross interfacial failure begins by the growth of a nanoscale gas bubble[14,15], driven by the internal gas pressure P, that plastically deforms the capping oxide layer to cause a visible outward blister (with radius of curvature, R). Existing models[14,16–18] pitch P against the yield strength σ_Y, of the MO layer, and its surface energy γ. One can then derive a critical blister radius R_C that depends on P, with the following relationship defining when blistering can occur:

$$P - \frac{4\sigma_Y t^2}{3R_C^2} - \frac{2\gamma}{R_C} > 0 \qquad (1)$$

where t is the MO layer thickness. However, after inserting reasonable material parameters into equation (1) (see Supplementary Information) for Al/Al_2O_3, the following problem is noted. For P values of a few hundred megapascals (same order as the bulk yield strength of Al), R_C is of the order of tens of nanometres. But if so, how does a 'subcritical' ($R < R_C$) gas bubble grow? Calculations show that the thermal fluctuation energy $k_B T$ cannot propel R to R_C within the experimental timescale. If one uses an unrealistically high gas pressure P of tens of gigapascals (even higher than the ideal strength of Al), R_C can still only be reduced to a few nanometres. In other words, existing theories, although explaining MO blistering at above tens of nanometres, seem to leave a gap below tens of nanometres, where M deformation seems inevitable.

This gap in understanding can be filled by recognizing that the metal surface morphology can change in the presence of free surface diffusion, which has been recently shown to be an important deformation mechanism of metals at sub-10-nm scale even at room temperature[19,20]. This speculation is strengthened by the realization that the metal configuration near M/MO is likely to be a metastable, kinetically trapped structure, usually not optimal for M itself in terms of its surface energies. However, if hydrogen atoms segregate to the M/MO interface and sever M–O bonds[21–23], the M atoms freed from MO can diffuse more quickly towards the desired shape, dictated by M's Wulff construction, at least at the nanoscale. This provides an additional thermodynamic driving force unaccounted for in equation (1), which is concerned with only oxide properties, as well as a kinetic pathway to achieve R_C because metal surface diffusion is very efficacious at changing morphology at small length scales (rate $\propto r^{-3}$; ref. 20). The postulated pathway is illustrated in Fig. 1. When an interface is weakened by the interface-segregating hydrogen atoms (Fig. 1a), surface diffusion of metal atoms becomes readily activated, to reshape the metal surface: the M atoms diffuse away along the M/MO interface to evolve the exposed M surface towards that predicted by the Wulff construction. Once the inwardly growing cavity (Fig. 1b) reaches a critical size, the trapped gas pressure will be sufficient to mechanically push the oxide layer outward. This permits the ensuing oxide blistering (Fig. 1c) that expands outward, causing eventual oxide spallation.

To directly observe how the cavity emerges initially underneath the oxide layer, here we have monitored the hydrogenation process of single-crystalline aluminium pillars with a thin layer of native oxide, in a 2 Pa H_2 gas environment at room temperature, inside an environmental transmission electron microscope (TEM). Figure 2 shows the bright-field TEM images of a pillar 240 nm in diameter, before and after hydrogen exposure. Two main changes can be clearly observed after exposure to hydrogen: the originally smooth thickness contours and metal/oxide interface have become wavy; blisters form at geometrical edges (red arrows in Fig. 2b). For comparison, *in situ* TEM experiments were also conducted in vacuum and with a pure nitrogen gas environment, which showed no such changes in the pillar under similar electron-beam intensity and exposure time, indicating that hydrogen exposure is responsible for the observed blistering and roughening. The main effect of the electron beam in our experiments is to ionize the H_2, generating high fugacity to facilitate hydrogen entrance[17].

Figure 3 reveals how the cavities nucleate at the metal/oxide interface. As seen in Fig. 3a, the initial interface is straight and smooth, and so are the thickness contours inside the pillar. As exposure to

[1]Center for Advancing Materials Performance from the Nanoscale (CAMP-Nano) & Hysitron Applied Research Center in China (HARCC), State Key Laboratory for Mechanical Behavior of Materials, Xi'an Jiaotong University, Xi'an 710049, China. [2]Department of Nuclear Science and Engineering, Cambridge, Massachusetts 02139, USA. [3]Department of Materials Science and Engineering, Massachusetts Institute of Technology, Cambridge, Massachusetts 02139, USA. [4]Department of Materials Science and Engineering, Johns Hopkins University, Baltimore, Maryland 21218, USA.
*e-mail: liju@mit.edu; ema@jhu.edu; zwshan@mail.xjtu.edu.cn

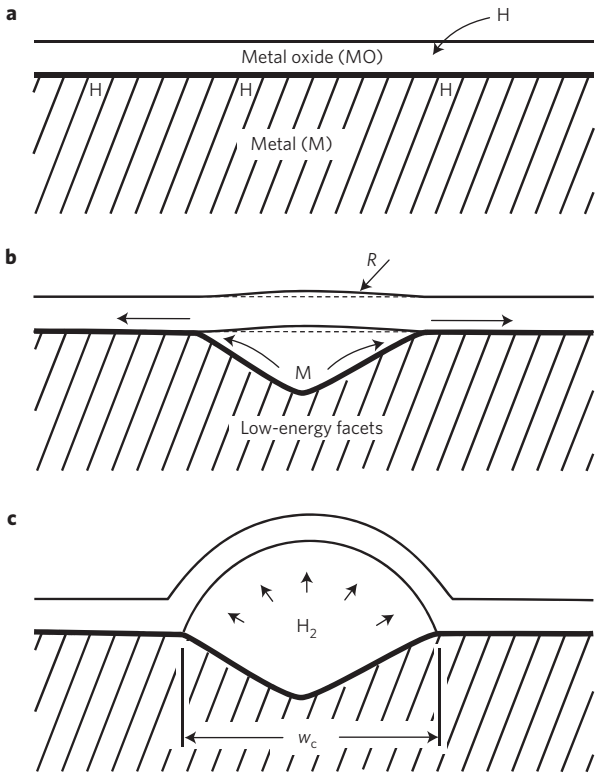

Figure 1 | Schematic illustration of the development of a blister on a metal surface. a, Hydrogen atoms segregated at the MO/M interface undermine the interfacial bonds. **b**, The metal locally reshapes itself by surface diffusion to approach the Wulff morphology, creating a cavity with low-energy facets at the metal side. **c**, After the cavity reaches a critical size w_c, the internal gas pressure becomes adequate to bend the MO layer outwards to form a dome-shaped blister of radius r.

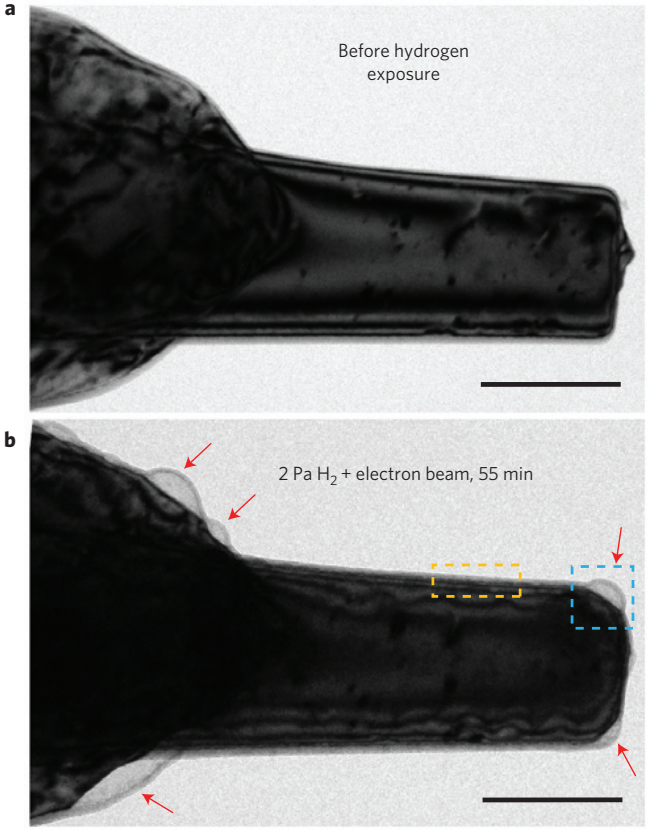

Figure 2 | Sample morphology before and after hydrogen exposure. a, The Al pillar before hydrogen exposure exhibits smooth thickness contours. **b**, The same pillar after hydrogen and electron-beam exposure for 55 min grows out several large blisters, as marked with red arrows. The thickness contours became wavy as well. The areas outlined by the orange and blue dashed lines are shown in Figs 3 and 4, respectively. Both scale bars, 200 nm.

hydrogen continues, small perturbations appear and grow to assume well-shaped cavities, which bow towards the metal side (see Fig. 3b and Supplementary Movie 1). The base widths w of these 'wells' range from a few nanometres to about 25 nm, and their spatial arrangement shows some degree of periodicity along the interface. The average cavity size characterized by $\bar{w}$ increases with time, and each individual cavity continuously changes its size and shape (see Supplementary Movies 1 and 2). Also, we observed cavity coarsening; that is, big cavities consume the small ones (see Supplementary Fig. 1). This evolution of nanocavities changes the thickness gradient in the near-interface region, giving rise to wavy thickness contours. As dislocation activity is not observed, the formation of the cavity at the oxide/metal interface is made possible by diffusional deformation of the metal surface. The surface diffusion is facile, because when hydrogen segregates at the interface, the interfacial atomic bonds are much weakened owing to hydrogen insertion[21–23], and the activation barrier for diffusion of the near-interface atoms is lowered because they are no longer directly bonded to the oxide. The metal surfaces are then able to locally approach the inclinations dictated by the Wulff construction, due to capillary forces that drive energy minimization. Consequently, {111} facets, which are known to have the lowest surface energy in face-centred cubic metals, are expected to develop. Indeed, as the cavities grow to about $w = 20$ nm in size (defined by the largest geometric dimension), their profiles show clear straight segments, which result from the projections of {111} facets that comprise the inner cavity surface bordering the Al underneath (Fig. 3c,d).

The above observations prove that low-gas-pressure cavity formation is made possible by the additional thermodynamic force of metal-side Wulff reconstruction, and also enabled by facile metal-side surface diffusion. In principle, as long as there is enough hydrogen segregation to debond M–O at the M/MO interface—a molecular (Ångström)-scale process that promotes freed-metal surface diffusion—such pre-blister nanoscale cavities can form, even with $P \to 0$.

Figure 4 depicts a typical process of blister formation at an edge of the pillar. After metal atoms diffuse away to leave a cavity, the newly exposed metal surfaces develop crystallographic {111} facets. Within 25 min of hydrogen exposure, the cavity w grows bigger as the {111} facets retreat inward, but the oxide layer remains unyielding (Fig. 4b). At 28 min, when the width of the cavity reaches 44 nm in diameter (Fig. 4c), the oxide begins to undergo large plastic deformation under the pressure of the accumulated H_2 gas, creating a blister.

Obviously, the cavity has to reach a critical size (w_c) before the onset of plastic deformation of the oxide layer, because it acts as a pinning constraint on the MO membrane. The initial stage of cavity emergence described above (not due to high internal hydrogen pressure) allows the deformation of the oxide layer to start from a much larger size than those required by traditional pressure-driven models[14,16–18]. Therefore, the singularity problem in those nucleation models is resolved. Also, this criterion underscores two directions that may help suppress the unwanted blistering. The first is to increase R_c by lowering the environmental hydrogen fugacity (such as lowering the level of moisture). The second is to decrease w_c by: reducing M surface reconstruction tendency, through

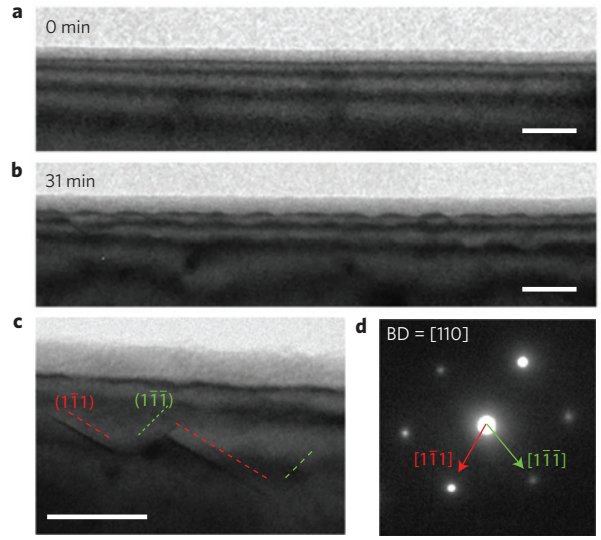

Figure 3 | Cavity nucleation and growth below the metal/oxide interface. **a**, Before exposure to hydrogen the initial interface is smooth. **b**, After 31 min of hydrogen exposure, the interface developed a wavy morphology (see Supplementary Movies 1 and 2). **c**, The grown cavities show clear {111} facets. **d**, The selected area diffraction pattern with the beam direction (BD) along the [110] zone axis of the pillar. All scale bars, 20 nm.

reducing surface roughness, removing grain boundary/surface intersections, and engineering the surface orientation; suppressing surface diffusion, possibly by adding alloying elements into the base metal.

The retreating {111} facet at the edge of the pillar also gives us an opportunity to quantitatively estimate the surface diffusivity. By drawing an analogy to the flattening of a wrinkled surface, a quantitative model to estimate the surface diffusivity can be obtained, following the method of refs 24,25. Assuming that the corner is a single-hump wrinkle, we can adopt the final rest position of the {111} facet in Fig. 4d as the reference and measure the height change of the receding facet with time. As plotted in Fig. 4e, the natural logarithm of height is a linear function of time, giving a slope of S. The surface diffusivity D_S can then be estimated using the following equation:

$$D_S = -\frac{Sk_BT}{\nu\gamma_M\Omega^2}\left(\frac{\lambda}{2\pi}\right)^4$$

where k_B is the Boltzmann constant, γ_M is surface energy of the metal ($\gamma_{M(111)} = 980\,\mathrm{mJ\,m^{-2}}$), Ω is atomic volume (0.0166 $\mathrm{nm^3}$/atom), T is temperature (298 K), ν is the surface atomic density ($\nu_{(111)} = 0.1\,\mathrm{atom\,nm^{-2}}$), and λ is the segment length of the facet in the rest position (for example, $\lambda = 50$ nm for the blister in Fig. 4d). The calculated D_S for the two individual blisters (Fig. 4 and Supplementary Fig. 2) is $2 \times 10^{-11}\,\mathrm{cm^2\,s^{-1}}$ and $3 \times 10^{-11}\,\mathrm{cm^2\,s^{-1}}$, respectively. This is very close to the prediction from the empirical rule[26,27],

$$D_S = 0.014\exp\left(\frac{-6.54T_m}{T}\right)\mathrm{cm^2\,s^{-1}}$$

where T_m is the melting temperature of Al (933 K). The calculated D_S is $1.8 \times 10^{-11}\,\mathrm{cm^2\,s^{-1}}$ for Al (without Al_2O_3) at room temperature. The pristine metal surfaces in our experiments are completely immersed in hydrogen, akin to clean Al with near-intrinsic surface diffusivity. We can therefore conclude that it is indeed the surface diffusion of Al that opens up the initial cavity for the blisters to take shape.

The degree of blistering we observed depends on surface orientation. Figure 5 shows scanning electron microscopy (SEM) images of a [110] (its axial direction) pillar, with Fig. 5a,b being the side view and top view, respectively. The orientations of the {111} planes (marked red) are shown in Fig. 5b. We observed that around the pillar circumference the blisters preferentially reside atop the {111} planes, whereas much smaller blisters are visible on the {100} planes and no blisters are found on the {110} planes. In comparison, Fig. 5c shows a pillar in the [100] axial direction, which has no {111} planes on its cylindrical surface. As a result, blisters form more randomly all over the cylindrical surface after prolonged hydrogen exposure. These results (see more evidence in Supplementary Fig. 3 and Supplementary Table 1) indicate that the surface blistering propensity is orientation dependent and follows the following ranking order: {111} > {100} > {110},

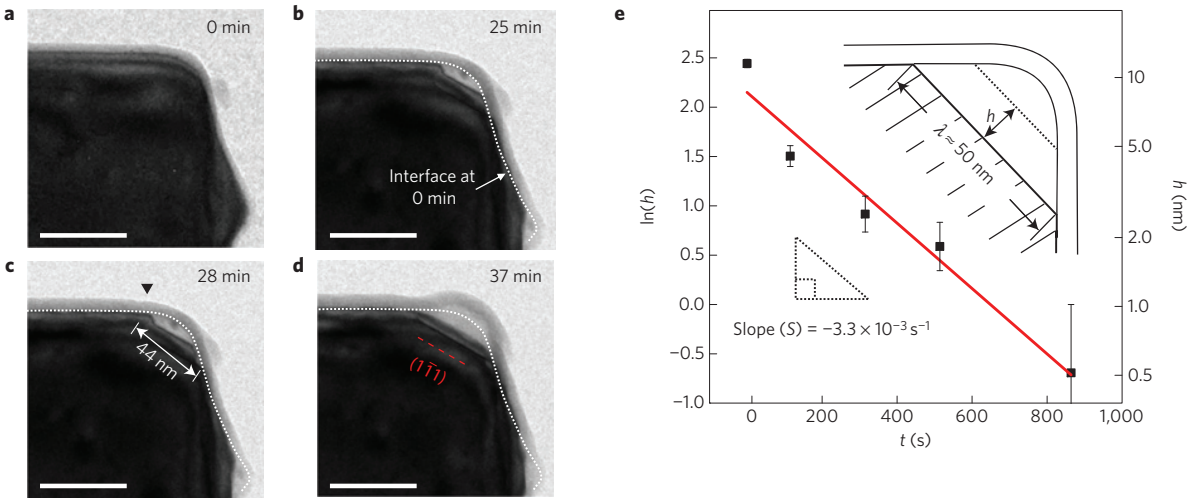

Figure 4 | Blister formation accompanying the receding faceted surface. **a**, The initial metal/oxide interface near an edge of the pillar; this reference profile of the interface is superimposed in **b**–**d** using a white dotted line. **b**, Cavity nucleation at the edge, with the metal surface retracted. Note that the oxide layer remains un-deformed at this point in time. **c**, The oxide layer bulges outward as a result of H_2 pressure. **d**, A ripened blister, with the oxide layer and metal surface bulging outward and inward, respectively. The newly exposed metal surface shows clear {111} facets. (See Supplementary Movie 1.) **e**, The measured retreating distance h of the {111} faceted surface versus exposure time (error for h measurements, ±0.5 nm). All scale bars, 50 nm.

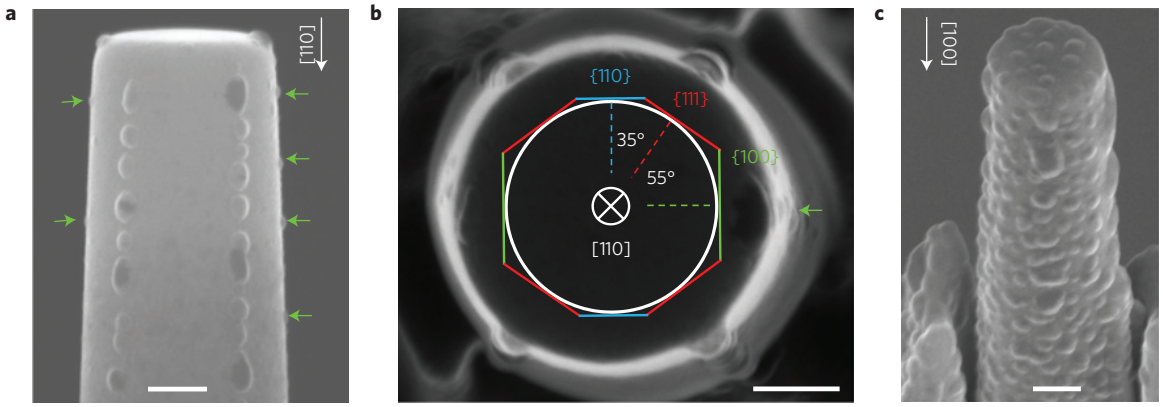

Figure 5 | Orientation-dependent blister distribution. a, Side-view SEM image of the pillar with the axis in the [110] direction after hydrogen exposure (~2 Pa, 35 min). Two columns of large blisters line up on the front surface. Additionally, small blisters exist at sites marked with green arrows. **b**, Top-view SEM image of the same pillar showing that four blister line-ups reside on the {111} surfaces, whereas small blisters reside on the {100} surfaces. **c**, Blisters on a pillar with [100] axial direction after hydrogenation (2–4 Pa, 1.5 h). Owing to the absence of {111} planes parallel to the pillar axis, blisters spread more randomly over the entire cylindrical surface. All scale bars, 200 nm.

in line with the expectation from their surface energies[28]. This blistering anisotropy originates from the fact that {111} facets have the lowest surface energy and are correspondingly the most prone to cavity nucleation and growth. As already shown in Fig. 4, the cavity on {111} has the fastest growth rate and reaches w_c the earliest. Figure 5 thus suggests that to delay blistering in the surface oxide, the metal should avoid low-energy planes parallel to its surfaces.

We have discovered that long before visible blisters are created, cavities form beneath the oxide film on hydrogen exposure, driven by Wulff reconstruction and freed-metal surface diffusion. We name this phenomenon 'pre-blister cavitation', which occurs on the metal side. Our findings suggest that it takes much less hydrogen to weaken the interface to allow Wulff reconstruction than to blister the oxide layer. This has implications for understanding the integrity/damage of coatings and passivation films on metals, where hydrogen-induced interfacial failure is a major threat. In particular, even when the blisters stay subcritical (Fig. 1b) owing to very small Wulff cavities (say ~5 nm), these very small Wulff cavities are still hidden damage that greatly reduces the interfacial delamination strength, by providing potential nucleation and coalescence sites for interfacial fracture under external stress. Therefore, blistering is a final-stage visible symptom of hydrogen damage of the interface, but not a necessary condition for markedly easier scale spallation from the substrate[6,29].

Methods

Methods and any associated references are available in the online version of the paper.

Received 5 February 2015; accepted 25 May 2015; published online 29 June 2015

References

1. Rozenak, P. Hemispherical bubbles growth on electrochemically charged aluminum with hydrogen. *Int. J. Hydrog. Energy* **32,** 2816–2823 (2007).
2. Liu, Y. *et al.* Detachment of alumina films from aluminium by 100 keV H^+ ions. *Surf. Interface Anal.* **33,** 318–321 (2002).
3. Subanovic, M. *et al.* Blistering of MCrAlY-coatings in H_2/H_2O-atmospheres. *Corros. Sci.* **51,** 446–450 (2009).
4. Sergo, V. & Clarke, D. R. Observation of subcritical spall propagation of a thermal barrier coating. *J. Am. Ceram. Soc.* **81,** 3237–3242 (1998).
5. Saunders, S. R. J., Monteiro, M. & Rizzo, F. The oxidation behaviour of metals and alloys at high temperatures in atmospheres containing water vapour: A review. *Prog. Mater. Sci.* **53,** 775–837 (2008).
6. Smialek, J. L. Moisture-induced TBC spallation on turbine blade samples. *Surf. Coat. Technol.* **206,** 1577–1585 (2011).
7. Haynes, J. A., Unocic, K. A. & Pint, B. A. Effect of water vapor on the 1100 °C oxidation behavior of plasma-sprayed TBCs with HVOF NiCoCrAlX bond coatings. *Surf. Coat. Technol.* **215,** 39–45 (2013).
8. Hultquist, G., Tveten, B. & Hornlund, E. Hydrogen in chromium: Influence on the high-temperature oxidation kinetics in H_2O, oxide-growth mechanisms, and scale adherence. *Oxid. Met.* **54,** 1–10 (2000).
9. Bailey, P. *et al.* Damage of alumina films by medium energy hydrogen and helium ions. *Nucl. Instrum. Methods Phys. Res. B* **197,** 265–270 (2002).
10. Tokunaga, K. *et al.* Blister formation and deuterium retention on tungsten exposed to low energy and high flux deuterium plasma. *J. Nucl. Mater.* **337,** 887–891 (2005).
11. Lu, G. H., Zhou, H. B. & Becquart, C. S. A review of modelling and simulation of hydrogen behaviour in tungsten at different scales. *Nucl. Fusion* **54,** 086001 (2014).
12. Scamans, G. M. & Rehal, A. S. Electron metallography of the aluminium-water vapour reaction and its relevance to stress-corrosion susceptibility. *J. Mater. Sci.* **14,** 2459–2470 (1979).
13. Sznajder, M. & Geppert, U. in *Advances in Solar Sailing* (ed. Macdonald, M.) Ch. 35, 559–571 (Springer, 2014).
14. Condon, J. B. & Schober, T. Hydrogen bubbles in metals. *J. Nucl. Mater.* **207,** 1–24 (1993).
15. Liu, Y. L. *et al.* Vacancy trapping mechanism for hydrogen bubble formation in metal. *Phys. Rev. B* **79,** 172103 (2009).
16. Flower, H. M. Electron-irradiation induced aqueous corrosion of aluminum and magnesium. *Radiat. Eff. Defects Solids* **33,** 173–179 (1977).
17. Bond, G. M., Robertson, I. M. & Birnbaum, H. K. On the determination of the hydrogen fugacity in an environmental cell TEM facility. *Scr. Metall.* **20,** 653–658 (1986).
18. Das, S. K. & Kaminsky, M. *Radiation Effects on Solid Surfaces* Vol. 158, Ch. 5, 112–170 (Advances in Chemistry, American Chemical Society, 1976).
19. Tian, L., Li, J., Sun, J., Ma, E. & Shan, Z. W. Visualizing size-dependent deformation mechanism transition in Sn. *Sci. Rep.* **3,** 2113 (2013).
20. Sun, J. *et al.* Liquid-like pseudoelasticity of sub-10-nm crystalline silver particles. *Nature Mater.* **13,** 1007–1012 (2014).
21. Oriani, R. A. & Josephic, P. H. Equilibrium aspects of hydrogen-induced cracking of steels. *Acta Metall.* **22,** 1065–1074 (1974).
22. Oriani, R. A. Hydrogen embrittlement of steels. *Annu. Rev. Mater. Sci.* **8,** 327–357 (1978).
23. Daw, M. S. & Baskes, M. I. Semiempirical, quantum mechanical calculation of hydrogen embrittlement in metals. *Phys. Rev. Lett.* **50,** 1285–1288 (1983).
24. Mullins, W. W. Flattening of a nearly plane solid surface due to capillarity. *J. Appl. Phys.* **30,** 77–83 (1959).
25. Keeffe, M. E., Umbach, C. C. & Blakely, J. M. Surface self-diffusion on Si from the evolution of periodic atomic step arrays. *J. Phys. Chem. Solids* **55,** 965–973 (1994).
26. Tu, K. N. *Solder Joint Technology* Vol. 117, Ch. 8, 211–243 (Springer Series in Materials Science, Springer, 2007).
27. Shewmon, P. *Diffusion in Solids*, Ch. 6, 189–222 (Minerals, Metals & Materials Society, 1989).

28. Vitos, L., Ruban, A., Skriver, H. L. & Kollar, J. The surface energy of metals. *Surf. Sci.* **411,** 186–202 (1998).
29. Leyens, C., Fritscher, K., Gehrling, R., Peters, M. & Kaysser, W. A. Oxide scale formation on an MCrAlY coating in various H_2–H_2O atmospheres. *Surf. Coat. Technol.* **82,** 133–144 (1996).

Acknowledgements

The authors acknowledge support from the Natural Science Foundation of China (51231005, 11132006, 51401159 and 51321003), and 973 Programs of China (2012CB619402). We also appreciate the support from the 111 project (B06025). J.L. acknowledges support by NSF DMR-1120901 and DMR-1410636. E.M. acknowledges support from US DoE-BES-DMSE, under Contract No. DE-FG02-09ER46056. We also thank P. H. Lu and M. Li for assistance in EELS characterization and data processing.

Author contributions

Z.-W.S., J.L. and E.M. conceived and designed the project. D.-G.X. conducted the experimental work. D.-G.X., Z.-W.S., J.L. and E.M. wrote the paper. All authors contributed to discussions of the results.

Additional information

Supplementary information is available in the online version of the paper. Reprints and permissions information is available online at www.nature.com/reprints. Correspondence and requests for materials should be addressed to J.L., E.M. or Z.-W.S.

Competing financial interests

The authors declare no competing financial interests.

Methods

We prepared single-crystal cylindrical aluminium pillars using focused ion beam (FIB) micromachining, such that various lattice planes in a chosen zone axis could occupy their representative areas on the cylindrical surface. This makes it convenient for investigating the effect of crystal orientation on the blistering behaviour. Also, unlike the acute wedge shape of an electrochemically polished sample, the cylindrical sample has a controllable surface curvature, edge-on to the electron beam, and thus is more conducive to imaging and visual observation.

Two types of cylindrical pillar, with an axial direction of either [110] or [100], were fabricated. All pillars had top diameters ranging from 220 to 500 nm, with an aspect ratio (height/diameter) between 2 and 3. To minimize the FIB damage, the final milling current was lowered to 2.34 pA. The as-fabricated pillars had a surface oxide layer (Supplementary Fig. 5) of about 5–9 nm in thickness.

The experiments were conducted in an environmental TEM (Hitachi H9500) evacuated to a base vacuum of 10^{-4} Pa. Ultrahigh-purity H_2 (99.999%) was introduced through a needle valve into the specimen chamber. The pressure was controlled in the range between 1 and 3 Pa, measured by a vacuum gauge near the sample. The intensity of the electron beam illuminating the pillar was 0.2–5.0 nA μm^{-2}, and the beam direction was close to the [110] direction of all pillars. The cavity formation and blistering processes were monitored using a Gatan 832 camera at 5 frames per second.

nature materials

SUPPLEMENTARY INFORMATION

DOI: 10.1038/NMAT4336

In situ study of the initiation of hydrogen bubbles at the aluminium metal/oxide interface

De-Gang Xie[1], Zhang-Jie Wang[1], Jun Sun[1], Ju Li[1,2*], Evan Ma[1,3*], Zhi-Wei Shan[1*]

[1] *Center for Advancing Materials Performance from the Nanoscale (CAMP-Nano) & Hysitron Applied Research Center in China (HARCC), State Key Laboratory for Mechanical Behavior of Materials, Xi'an Jiaotong University, Xi'an 710049, China*

[2] *Department of Nuclear Science and Engineering and Department of Materials Science and Engineering, Massachusetts Institute of Technology, Cambridge, Massachusetts 02139, USA*

3 Department of Materials Science and Engineering, Johns Hopkins University, Baltimore, MD 21218, USA

*e-mail:liju@mit.edu (J.L.), ema@jhu.edu (E.M.), zwshan@mail.xjtu.edu.cn (Z.S)

DOI: 10.1038/NMAT4336

Cavity coalescence

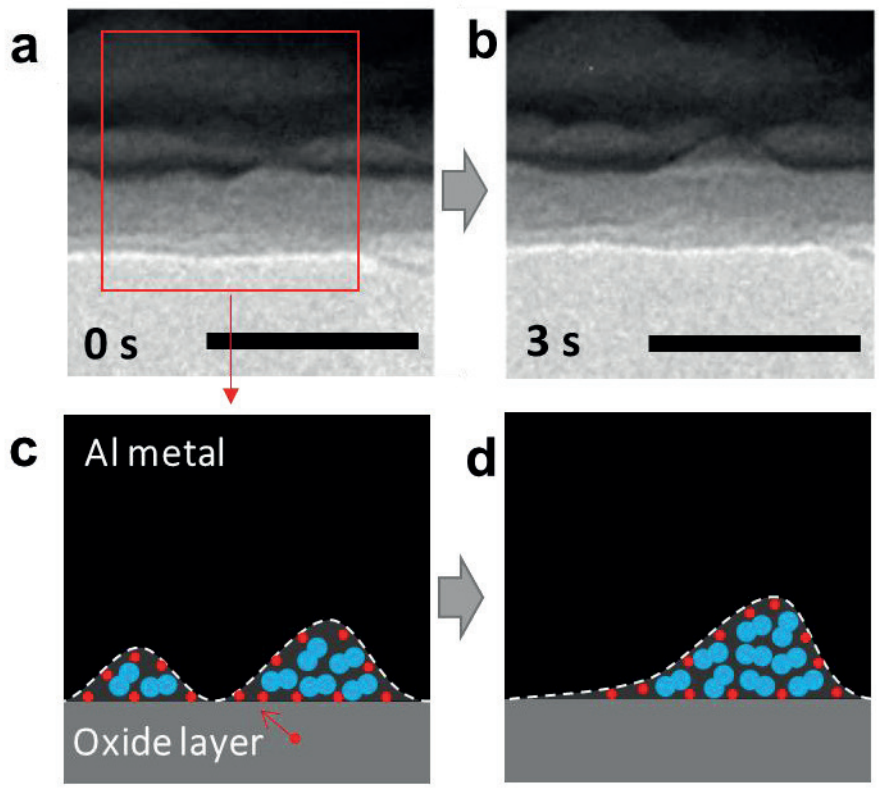

Figure S1 A typical coalescence process of two cavities. a-b are snapped images and **c-d** are corresponding schematic illustration of the area boxed in **a**. Two neighboring hydrogen-filled cavities in **a** and **c** were bridged up and combined to produce one big cavity in **b** and **d**. Both scale bars are 20 nm.

Pressure calculation

If the blister deforms plastically, then the internal pressure can be estimated by the following equation[1]:

$$P_{\sigma_y} = \frac{4\sigma_y t^2}{3r^2} \quad (1)$$

in which, σ_y is the yield stress of the oxide layer (3 GPa is used, refers [2]), t is the thickness of oxide layer (7.5 nm in Figure 4-d), and r is the radius of curvature of the blister (r=22 nm in Figure 4-d). The calculated internal pressure is 464 MPa.

Due to the small size of the bubble, the effect of surface tension should be considered.

If deformation of the blister lid is viscous[3], the hydrogen gas pressure in the blister is thus determined by surface energy and blister radius according to the following equation:

$$P_{\gamma} = 2\gamma / r \tag{2}$$

in which γ is the surface energy ($\gamma_{(111)}$=980mJ/m^2), r is blister radius. For the blister with r=22 nm in Figure 4-d, this method gives a pressure to be 84 MPa. The real pressure should be the sum of plastic yield and viscous flow, which give a value of 548 MPa. In contrast, if we assume a nuclei radius of 1 nm, the required pressure would be 198 GPa by taking the same estimating method. It is apparently unrealistic high. Therefore, a critical size above which the internal hydrogen pressure can afford deforming the oxide layer is necessary.

Diffusivity calculation

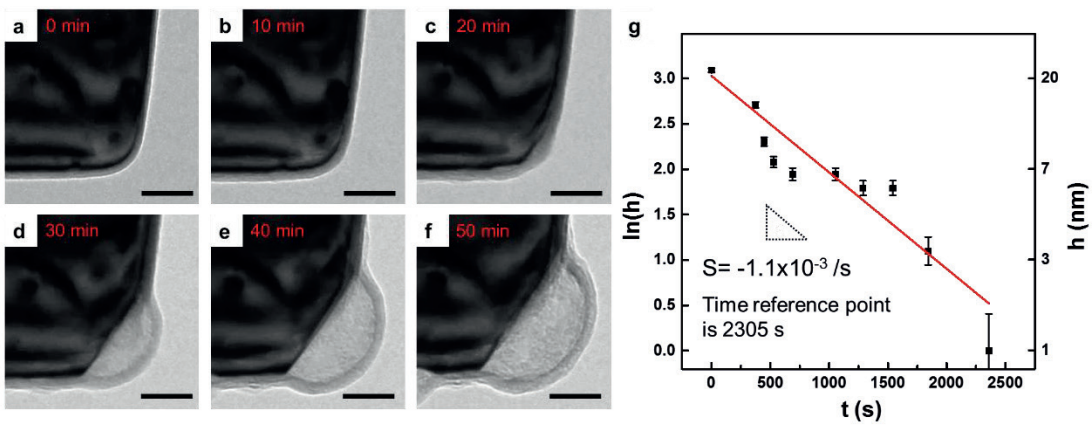

Figure S2 The measurement of another blister. a-f, are sequence images displaying the blister growth process accompanied with a retreating {111} facet. **g**, measured height change of the {111} facet vs. time. All scale bars are 20 nm.

Reproducibility of the orientation-dependent blistering

DOI: 10.1038/NMAT4336

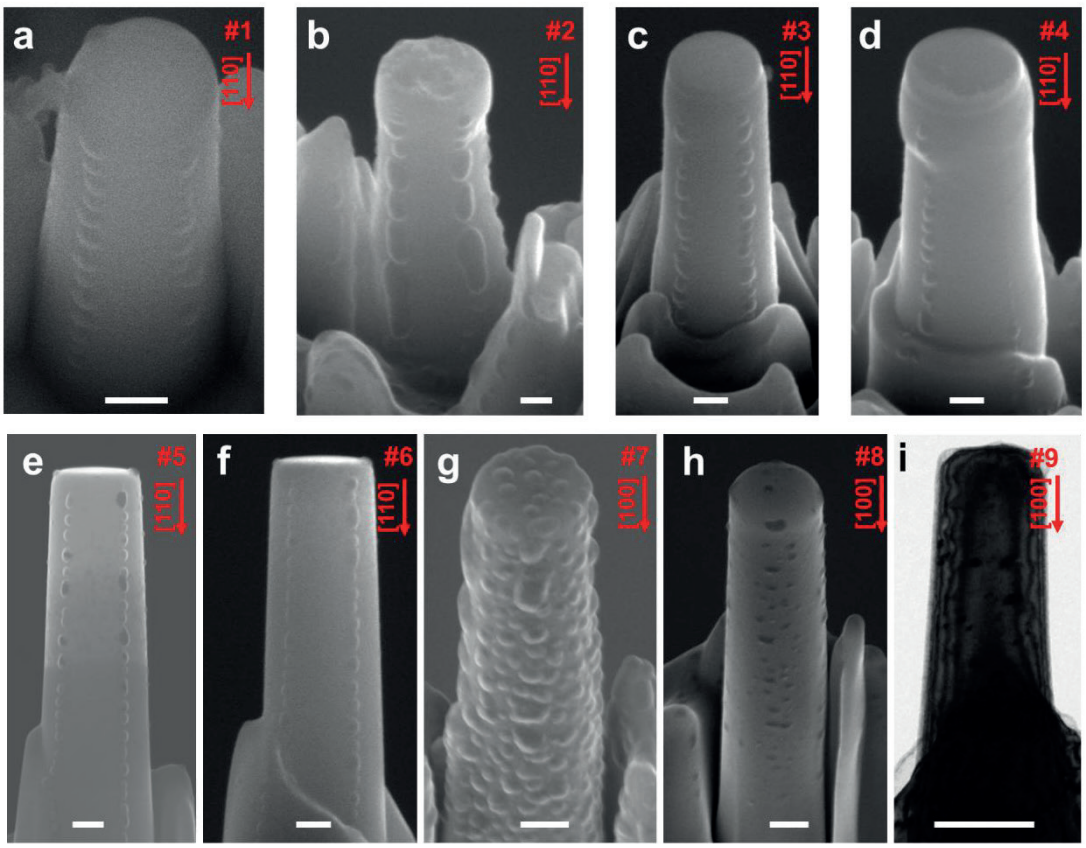

Figure S3 Morphology of all hydrogenated samples demonstrating the good reproducibility of orientation-dependent blistering. **a-f** are pillars with [110] axial direction. **g-i** are pillars with [100] axial direction. All scale bars are 200 nm

Table S1 Hydrogenation conditions for pillars shown in Figure S3

Sample	H2 pressure(Pa)	Exposure time@ Beam Intensity(nA/μm^2)
#1	2– 3	1 h@0.68
#2	2-3	22 min@0.45 + 1.5 h@0.054
#3	2-3	30 min@0.45 + 1 h@0.048
#4	2-3	25 min@0.45 + 23 min@0.048
#5	1.8-2.2	35 min@0.83
#6	1.8-2.2	20 min@0.49 + 22 min@0.83
#7	2-4	1.5 h@0.68
#8	2-3	1 h@0.68
#9	1.7-2.5	15 min@0.2 + 25 min@0.4 + 6 min@1.5 + 5 min@5.0

Hydrogen assisted peeling-off of thin oxide film

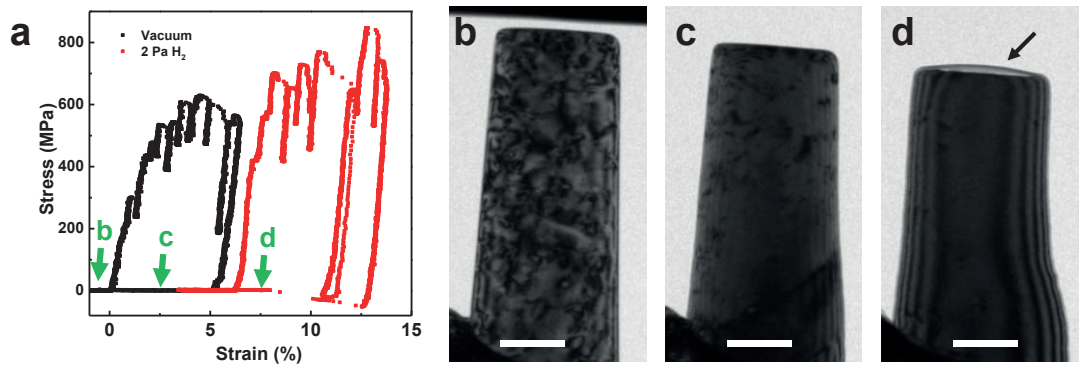

Figure S4, **An example of hydrogen assisted peeling-off of a thin oxide film. a**, stress-strain curves of two successive tests in vacuum (black) and in 2 Pa hydrogen gas (red) of an aluminum pillar. (**b**)-(**d**) are bright field TEM images of the pillar at moments marked with green arrows in (**a**). Compared with the image after compression in vacuum (**c**), obvious oxide layer delamination is observed after the compression test in hydrogen (**d**). All scale bars are 200 nm.

Chemical analysis of surface layer

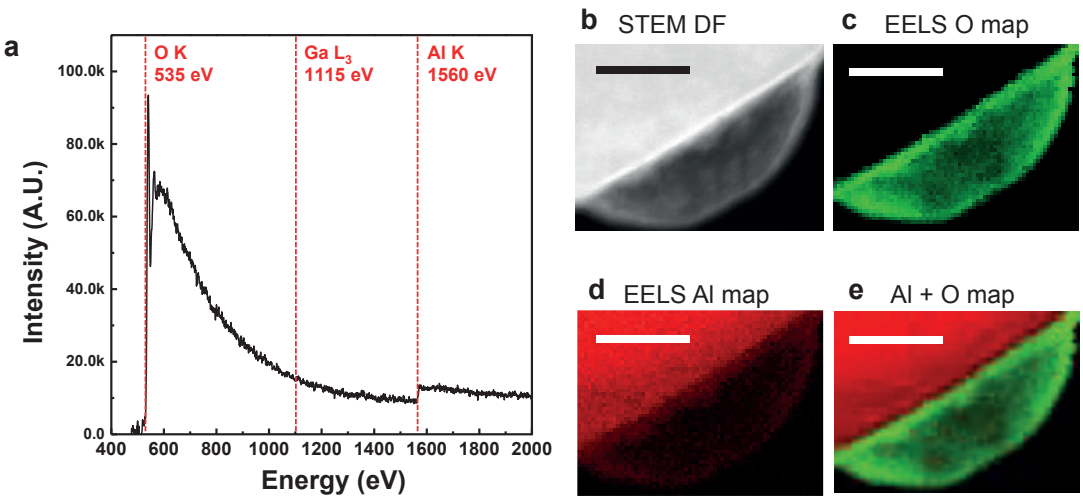

Figure S5 Chemical analysis of a blister with electron energy loss spectroscopy (EELS) technique. a, EELS spectrum taken from a blister in (**b**) shows clear O-K edges and Al-K edges, but no Ga-L_3 edges, indicating that FIB effect can be neglected in our experiments. **b**, the scanning TEM dark field image of the analyzed blister. **c** and **d** are the oxygen map and the aluminum map respectively extracted from energy-filtered TEM image. **e**, the overlap of oxygen map and aluminum map showing that the blister is aluminum oxide. All scale bars are 50 nm.

References

1 Turner, C. E. *Introduction to plate and shell theory*. 75 (American Elsevier Pub. Co., 1965).

DOI: 10.1038/NMAT4336

2 Tapily, K. *et al.* Nanoindentation investigation of HfO2 and Al2O3 films grown by atomic layer deposition. *J. Electrochem. Soc.* **155**, H545-H551 (2008).

3 Bond, G. M., Robertson, I. M. & Birnbaum, H. K. On the determination of the hydrogen fugacity in an environmental cell TEM facility. *Scripta Metall.* **20**, 653-658 (1986).